

# High-order harmonic generation via multicolor beam superposition

S. Sarikhani<sup>1</sup> · S. Batebi<sup>1</sup>

Received: 14 May 2017 / Accepted: 3 August 2017 / Published online: 19 August 2017  
© Springer-Verlag GmbH Germany 2017

**Abstract** In this article, femtosecond pulses, especially designed by multicolor beam superposition are used for high-order harmonic generation. To achieve this purpose, the spectral difference between the beams, and their width are taken to be small values, i.e., less than 1 nm. Applying a Gaussian distribution to the beam intensities leads to a more distinct pulses. Also, it is seen that these pulses have an intrinsic linear chirp. By changing the width of the Gaussian distributions, we can have several pulses with different bandwidths and hence various pulse duration. Thus, the study of these broadband pulse influences, in contrast with monochromatic pulses, on the atomic or molecular targets was achievable. So, we studied numerically the effect of these femtosecond pulses on behavior of the high-order harmonics generated after interaction between the pulse and the atomic hydrogen. For this study, we adjusted the beam intensities so that the produced pulse intensity be in the over-barrier ionization region. This makes the power spectrum of high-order harmonics more extensive. Cutoff frequency of the power spectrum along with the first harmonic intensity and its shift from the incident pulse are investigated. Additionally, maximum ionization probability with respect to the pulse bandwidth was also studied.

## 1 Introduction

The prominent way to study atomic or molecular dynamics is to expose these systems to an intense laser radiation.

Two most significant phenomena can take place under this exposure, are high-order harmonic generation (HHG) and above threshold ionization (ATI), where HHG is the best solution for producing attosecond pulses of extreme ultraviolet (EUV) [1, 2]. For more than two decades, scientists have been trying to produce attosecond pulses experimentally, or predict the behavior of these types of ultrashort pulses theoretically. The first experiments on the attosecond pulse production [3, 4], were performed on the basis of theoretical investigations previously developed [5–8]. In those experiments femtosecond pulses were radiated to the targets, including argon or neon gases. Although the most common and suitable underlying harmonic generation processes utilize atomic gas targets [9, 10]; however, molecules [11–13], plasma plumes [14–16], dielectric and metallic surfaces [17, 18], and solids [19] such as graphene flakes [20], and even bulk crystals [21, 22] have also been used for HHG. Because of the highly complicated theoretical studies in the case of heavy molecules, most of theoretical and numerical investigations considered the simplest atomic or molecular systems such as hydrogen (H) [23], helium ion (He<sup>+</sup>) [24, 25], hydrogen molecule or its ion molecule (H<sub>2</sub> or H<sub>2</sub><sup>+</sup>) or their isotopes [26–29], and so on. In these studies, several initial conditions such as peak intensity [30, 31] or wavelength of the pulse [32, 33], and also electric field's polarization [13, 34, 35] and its angle with respect to the axis of the molecule [36–38] are investigated. Furthermore, chirp effect on the oscillation frequency [25, 39–41], and the effect of the multicolority of the electric field [34, 39, 42], and even the initial energy level of the atom or molecule at the instant of the pulse impact [43, 44] have been studied. The results of these effects on the behavior of the extracted harmonics, and the attosecond pulses, both in one [39, 45] and three dimensional [27, 46] approaches, are investigated.

✉ S. Batebi  
s\_batebi@guilan.ac.ir

<sup>1</sup> Department of Physics, Faculty of Science, University of Guilan, P.O. Box 41335-19141 Rasht, Iran

High-order harmonics are generated from atoms or molecules through an ionization and recollision process described by the semi-classical so-called three-step model [1, 5, 6]. Radiation of the intense laser field of a femtosecond pulse to the atoms of a target results in extraction of high-order harmonics of the incident frequency, and in conclusion, an attosecond pulse train may be generated. EUV super continuum generation is a highly nonlinear process and deeply sensitive to slight changes in the color of the laser pulse.

In this article, we designed a broadband femtosecond laser pulse, by superposing too many continuous wave (CW) beams having a color difference and a width of less than 1 nm. It is not interesting to see that the superposition of CW beams gives rise to generation of a pulse. But surprisingly, it can be seen that the pulse duration is in the order of femtosecond. Also we observed that these femtosecond pulses have an intrinsic chirp. Essentially in this paper we planned to study how a broadband pulse, affects the HHG spectra and the other behaviors, related to the interaction of this pulse with the gaseous jet target of the atomic hydrogen. These types of pulses, however, have an essential difference with amplified spontaneous emission (ASE) pulses. In these types of pulses, all components of the pulse have arranged phase relations; for example, in this paper, they are locked at the zero phases. But, in an ASE pulse, the components are not in a phase relationship. Beam intensities have been distributed to a gaussian function, centered at 800 nm, and limited to 300–1300 nm area. These distributions have different full width at half maximum (FWHM) from 26 to 476 nm. It is noteworthy that for this study, HHG spectrums with broader plateaus are favorable. Thus, the peak intensities of pulses have been chosen to be in the over barrier ionization region, i.e.,  $I_0 > I_b^H$ , where for hydrogen-like atoms we can find that  $I_b = 4 \times 10^9 I_p^4 / Z^2$ , where  $I_b$  is the threshold ionization intensity in  $\text{W}/\text{cm}^2$ ,  $I_p$  is the ionization potential in eV, and  $Z$  is the charge state of the relevant atom. Thus, for hydrogen atom  $I_b^H = 140 \text{ TW}/\text{cm}^2$  as mentioned in [47]. In this work all of the pulse intensities have been set to be  $400 \text{ TW}/\text{cm}^2$ .

Pulse duration, behavior of the intrinsic chirp, behavior of recollision time and energy, maximum ionization probability, cutoff frequency in the power spectrum, intensity and location of the first harmonic spectrum, and also its shift from the incidental pulse in terms of different pulse widths, are investigated in this work. As it will be seen more clearly in subsequent sections, we clip the tail of the pulse when the amplitude of the electric field drops to about 2% of the maximum. Further tail of the pulse does not impose significant changes in the harmonic spectrum except for the intensities of the frequencies about  $7\omega_0$  and  $10\omega_0$ , at the beginning of the plateau.  $\omega_0$  is the frequency corresponding to 800 nm in wavelength. It is amazing to see that the tail of the pulse affects the spectrum, remarkably just, at these

two frequencies. The relative intensity of the spectrum, i.e.,  $I(\omega)/I(\omega_0)$ , at these two frequencies increases by the tail. To present these behaviors, we begin with the theoretical modeling, and subsequently, the results will be obtained by employing the numerical solution of the time dependent Schrödinger equation (TDSE).

## 2 Theoretical approach

In this paper, we investigate high-order harmonic generation by developing a special multicolor electric field based on the superposition of several electric fields whose wavelengths differ by a little constant value, and applying this electric field to a target of a hydrogen atom. In these types of calculation, we can consider the single active electron approximation (SAEA). We begin with introducing the field and subsequently the model of HHG. In this article, we used Hartree atomic units (a.u.), where the numerical values of the four fundamental physical constants ( $m_e$ ,  $e$ ,  $\hbar$ ,  $k_e = 1/4\pi\epsilon_0$ ) are all unity.

### 2.1 Electric field

In this study, we attempt to produce a femtosecond pulse with a linearly polarized electric field by superimposing many linearly polarized CW electric fields. Actually, we aim to produce broadband femtosecond pulses, with the following Gaussian wavelength distribution:

$$F(\lambda) = \exp\left(-4 \ln 2 \frac{(\lambda - \lambda_0)^2}{(\Delta\lambda)^2}\right). \quad (1)$$

$\lambda_0 = 800 \text{ nm}$  is the center and  $\Delta\lambda$  is the width of the spectrum. Indeed, we plan to produce  $F(\lambda)$  by superposing several CW beams having Gaussian bands as:

$$F(\lambda) = \sum_{m=1}^M c_m(\lambda), \quad (2)$$

$$c_m(\lambda) = AF(\lambda_m) e^{-\frac{(\lambda - \lambda_m)^2}{(\delta\lambda)^2}}, \quad (3)$$

where  $M$  is the total number of beams,  $A$  is a constant,  $\lambda_m$  is wavelength of the  $m$ th beam and  $\delta\lambda = \lambda_m - \lambda_{m-1}$  is the color separation of the beams. The value of  $\delta\lambda$  is taken to be a few nm or sub-nm in wavelength and the beams' spectral width is set to be about  $\delta\lambda$ . The beams' wavelengths ( $\lambda_m$ ) are taken from 300 nm [in the ultraviolet (UV) region] to 1300 nm [in the near-infrared (NIR) region]. Figure 1a shows Gaussian distributed intensities for the case when  $\Delta\lambda = 212 \text{ nm}$  and  $\delta\lambda = 10 \text{ nm}$ .

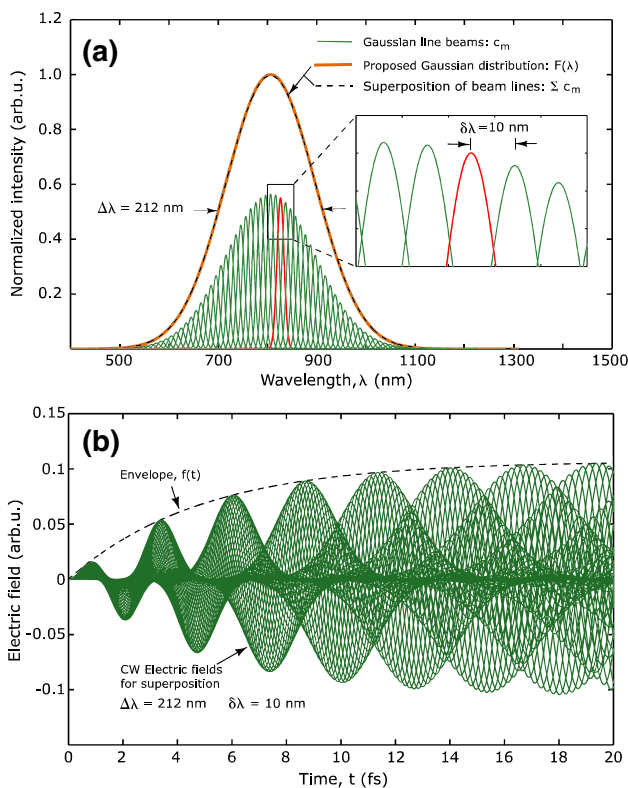


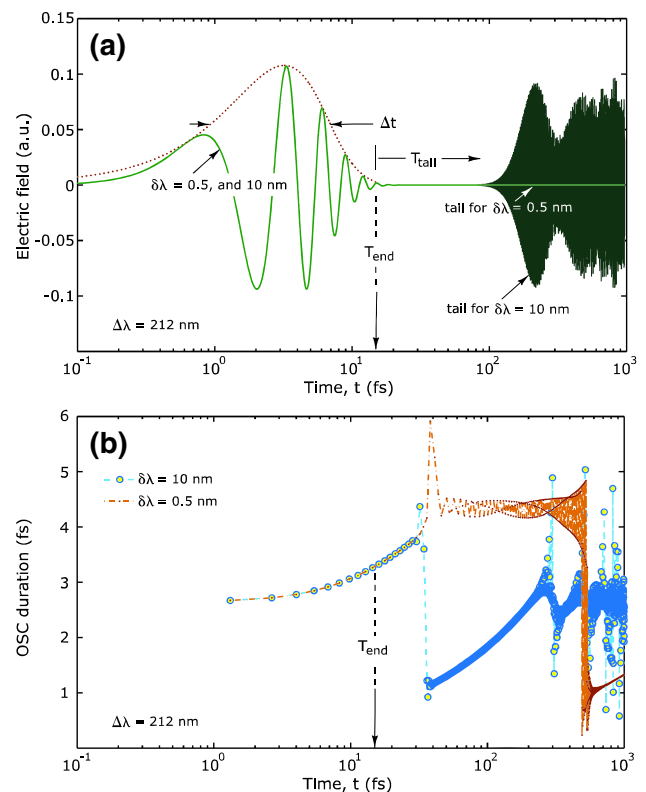
**Fig. 1** **a** By assuming the Gaussian distribution for each beam’s spectrum with a width of  $\delta\lambda$ , and color difference of  $\delta\lambda$ , the complete distribution of the main pulse spectrum,  $F(\lambda)$ , is reproduced by summing these narrow Gaussian functions. **b** The electric fields contributed to producing the final electric field. As can be seen, all of them are bounded to  $f(t)$ . In this figure  $\Delta\lambda$  is taken to be 212 nm, and  $\delta\lambda = 10$  nm

In Fig. 1b, we have plotted all electric fields with different wavelengths and amplitudes related to Fig. 1a. According to Eqs. (2, 3), the amplitude of  $m$ th electric field is proportional to  $F(\lambda_m)$ . Thus, we can write the total electric field as:

$$E(t) = a_0 f(t) \sum_{m=1}^M \sin(\omega_m t) F(\lambda_m). \tag{4}$$

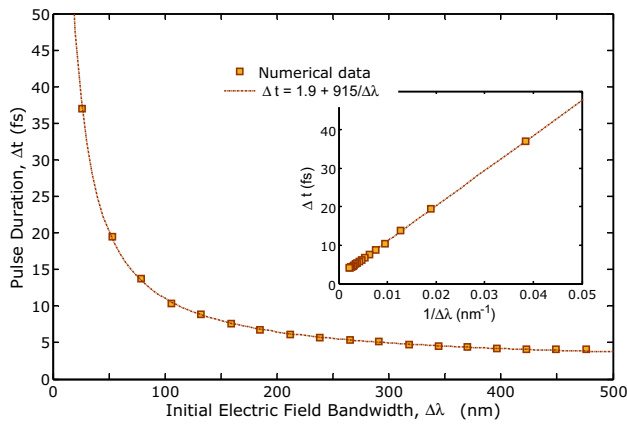
Here,  $a_0$  is a constant defined in the way that the maximum amplitude of the total electric field to be  $E_0 = 0.107$  a.u., related to the peak intensity of  $400 \text{ TW/cm}^2$  ( $4 \times 10^{14} \text{ W/cm}^2$ ), and also  $\omega_m = 2\pi c/\lambda_m$ , where  $c$  is the speed of light in vacuum, and  $f(t) = 1 - \exp(-0.005t)$  is introduced to shape the rising part of the pulse as smooth as possible.

Figure 2a represents the resulted electric fields with  $\Delta\lambda = 212$  nm and for two cases of  $\delta\lambda = 10$  nm and  $\delta\lambda = 0.5$  nm. It is worthy of attention that the applicable head in both produced electric fields are the same, but, it is preferred to utilize the narrower lines ( $\delta\lambda = 0.5$  nm) due to perfectness of the tail. As can be seen in Fig. 2a end of the electric pulse is represented by  $T_{\text{end}}$ . We set  $T_{\text{end}}$  such



**Fig. 2** **a** Total electric field produced by the multicolor beam superposing for  $\Delta\lambda = 212$  nm and for two different values of  $\delta\lambda = 10$  nm, and  $\delta\lambda = 0.5$  nm. It is attractive to see that the main deduced and usable electric field is the same for both cases. The tail for both values of  $\delta\lambda$  is considered from  $T_{\text{end}}$  till it is desired, before distortions take place.  $T_{\text{end}}$  is the instant when  $E(T_{\text{end}}) = 0.02 E_0$ . **b** Oscillation duration of electric fields corresponding to **a** versus time. This figure represents the intrinsic chirp for these types of electric fields

that the amplitude of the electric field drops to 2% of the maximum,  $E_0$ , or equivalently, when time reaches about 2.5 times as larger as the pulse duration ( $T_{\text{end}} = 2.5 \Delta t$ ). For further applications, the rest of the total electric field (distortion-free region) is defined to be the tail with duration of  $T_{\text{tail}}$ , which it can be adjusted for the desired values. Another remarkable feature of the produced electric field is the dependency of its oscillation duration on time. In other words, the electric field has an intrinsic chirp. Figure 2b shows this effect for two cases of  $\delta\lambda = 10$  nm and  $\delta\lambda = 0.5$  nm. It can be inferred from Fig. 2a that oscillation duration for both cases must coincide at least until the time  $T_{\text{end}}$ . Figure 3 depicts the behavior of the pulse duration versus the spectral pulse width. As can be deduced from this figure, the behavior of  $\Delta t$  with respect to  $1/\Delta\lambda$  is linear. This means that we can define a simple rational function of the form  $\Delta t = m + n/\Delta\lambda$  for this relationship. This is simply a consequence of the standard time-bandwidth product describing the pulse duration of a transform limited pulse based on a certain spectral width. In Fig. 4,



**Fig. 3** Pulse duration ( $\Delta t$ ), versus the spectral pulses width ( $\Delta\lambda$ ). Inset shows the pulse duration versus  $1/\Delta\lambda$ , which indicates that the pulse duration changes linearly with respect to  $1/\Delta\lambda$ . In this figure,  $\delta\lambda = 0.5$  nm

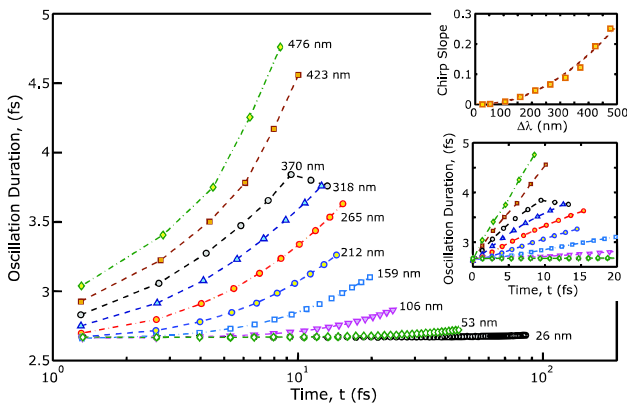


**Fig. 4** Oscillation duration of the pulse versus time (intrinsic chirp) for various  $\Delta\lambda$  in the effective part of the pulses (before  $T_{end}$ ). The quantities mentioned next to each curve represents  $\Delta\lambda$ . Time axis is in logarithmic scale for having all data in the window. In the inset the data are plotted so that the time axis is in linear scale. We can see the intrinsic chirp effect changes almost linearly in time. Thus, we calculated the slope of each curve and showed them in another figure in the inset. Also in this figure  $\delta\lambda = 0.5$  nm

we showed the intrinsic chirp of the pulses for different values of  $\Delta\lambda$ , and it can be seen in the inset of this figure, that the intrinsic chirp effect is almost linear in this time range. Each of the curves is plotted within the effective time of the pulse, i.e., from the beginning to  $T_{end}$ , when the chirp effect has not distorted yet. Slope of the linear chirp versus  $\Delta\lambda$  is also plotted in the inset of the figure. It has been shown in this figure that for lower  $\Delta\lambda$ , related to larger  $\Delta t$ , the oscillation duration changes very slowly in time. In other word, the chirp effect in the case of short  $\Delta\lambda$  can be ignored. As it can clearly be seen in these figures, by reducing  $\Delta\lambda$  to very small values in which the pulse has almost a certain frequency, the time duration of the

pulse tends to infinity at first, and secondly, the chirp effect vanishes. In other words, in this case, we have a single frequency CW beam, actually, we chose one of the beams. It is worthy of mention that this figure is independent of the peak intensity of the pulse.

Classical mechanics may help in analyzing the electron trajectory. In the semi-classical Simple Man's three-step model, the atomic potential is deformed due to strong laser field and electron can tunnel to the continuum.

In this model the calculations are made within the strong field approximation (SFA) neglecting the ion coulomb field for the propagation of a liberated electron. Additionally, the coulomb field is considering as a short range potential, therefore the trajectories of the electron start at the origin and also electron recombines with ion at the origin. Furthermore, this model assumes that the electron has zero velocity right after the tunneling process. Classical electric force, applying to a free electron by an external electric field  $E(t)$  is determined by  $m_e a(t) = -eE(t)$ , where  $m_e$  and  $e$  are the mass and charge of the electron, respectively, and  $a(t)$  is the acceleration of the free electron as it moves under the influence of the laser electric field. We assume that the electron ionization takes place at  $t_i$  and recombination of the electron with its parent ion takes place at  $t_r > t_i$ . Thus, velocity of this electron,  $v(t, t_i)$ , and its trajectories,  $r(t, t_i)$ , at every time  $t$  before  $t_r$  (i.e.,  $t_i \leq t \leq t_r$ ) in atomic unit can be obtained from  $v(t, t_i) = \int_{t_i}^t E(t') dt'$  and  $r(t, t_i) = \int_{t_i}^t dt' \int_{t_i}^{t'} E(t'') dt''$ , respectively. Multiphoton and tunneling ionization are two competing ionization processes that happen at low frequency [48]. The Keldysh parameter,  $\gamma$ , determines which process can happen:

$$\gamma(\omega) = \left[ \frac{I_p}{2U_p} \right]^{\frac{1}{2}} = \frac{\omega}{E_0} \sqrt{2I_p}, \tag{5}$$

where  $I_p$  is the ionization potential and for hydrogen atom  $I_p^H = 0.5$  a.u. or equivalently 13.6 eV.  $U_p$  represents the ponderomotive potential of the laser field  $U_p = I/4\omega^2$ ,  $\omega$  is the field frequency and  $E_0$  is the maximum amplitude of the field. According to this equation, the Keldysh parameter linearly depends on the frequency in this work. Figure 4 indicates that in all of these 10 cases of  $\Delta\lambda$ , oscillation periods changes between 2.7 and 4.8 fs. In other words, the frequency of these fields varies from 0.032 to 0.056 a.u., i.e., for  $I_0 = 400$  TW/cm<sup>2</sup>, or  $E_0 = 0.107$  a.u., in all cases  $\gamma < 1$ . This result, confirms that tunneling ionization is the dominant mechanism for these fields and also for higher fields. However, it can be found that the tunneling ionization threshold satisfies by  $I_0^{\min} = 111$  TW/cm<sup>2</sup> in this study. Again, we mention that, these results were obtained due to independency of Fig. 4 to the field strength. As mentioned above, the returning of the electron must take place at the

origin. So, we can find the recombination time  $t_r$  with respect to the ionization time  $t_i$  by solving the following equation

$$\int_{t_i}^{t_r} dt \int_{t_i}^t E(t') dt' = 0, \tag{6a}$$

and the recollision kinetic energy  $K(t_r, t_i)$  of electron, in atomic units, can be obtained as follows:

$$K(t_r, t_i) = \frac{1}{2} \left[ \int_{t_i}^{t_r} E(t) dt \right]^2. \tag{6b}$$

Figure 5a depicts the classical relation between recollision and ionization times for three typical values of  $\Delta\lambda = 106, 212,$  and  $423$  nm. Because of the similarity, we focus on the case  $\Delta\lambda = 212$  nm. Figure 5b shows the recombination energy of the electron versus time for this case. As we see in this figure there are two distinct profiles corresponding to recollision energy. Recombination and ionization profiles are corresponding to recombination energy versus  $t_r$  and  $t_i$ , respectively, i.e., when the recombination profile is under the study, the time scale represents  $t_r$  and vice versa. At first glance, this

figure shows that, for all cases, no recombination takes place before ionization time, consequently we should not expect any recombination before  $t_{r1} = 1.34$  fs, thus no recombination energy is predicted before this time as shown in recombination profile in Fig. 5b. As can be seen in Fig. 5a, there are no values for  $t_r$  in some periods of ionization times. These periods of times, represented by the blue (light gray) colored areas. It means that if an electron ionizes at the moment in these areas, it will not return to the parent ion, and thus, no recombination energy is predicted for this electron. This fact is also shown in Fig. 5b with blue (light gray) colored regions. We remember that these areas in this figure are related to the ionization profile. As we know, electrons that ionized earlier, recombine later. Due to this fact, we can assume short trajectories and long trajectories for the motion of free electrons in the laser electric field. For example, recombination energies related to the first trajectories of the electron are demonstrated in Fig. 5b, as  $ST^1$  (for 1st short trajectory) and  $LT^1$  (for 1st long trajectory). It can be understood from the ionization profile in this figure that, if the electron releases its parent ion in each ionization time represented by A, B, C, ..., it will return to the ion with maximum recombination energy. These points, can also be illustrated in the recombination energy versus  $t_r$  and  $t_i$ , respectively, as A', B', C', etc., and correspond to  $t_{r2} = 2.54$  fs,  $t_{r3} = 3.88$  fs,  $t_{r4} = 5.24$  fs, etc., respectively. These points, marked in Fig. 5a, are frontiers between short trajectories and long trajectories. Also it is worthy of mention that for some  $t_r$ , there are more than one  $t_i$ . For example, as is shown in Fig. 5a by a horizontal line, and in Fig. 5b by a vertical line, at  $t_{r4}$  we can recognize three different trajectories with various recombination energies for the electron returned to the ion. In other words, for example, the recombined electron at  $t_{r4}$  could be initially ionized at three different moments before, represented by C', C'', and C''' related to  $t_i = 0.49, 1.97,$  and  $3.49$  fs, respectively. Recombination energy of this electron determines its trajectory. This is because of the electron has more opportunities for recombination if it ionizes at C''' or C'' and or even at C' moment. For example, in Fig. 5a by drawing a vertical line passing through the C''' point, at about 0.5 fs, we see that there are three possibilities for the electron to recombine with its parent ion with three different recombination times. The later recombination corresponds to the smaller laser field amplitude, thus the electric force on the electron becomes smaller and hence the recombination energy of the electron is decreased. Briefly, we can describe the curves depicted in Fig. 5b point by point using the relations between ionization and recollision times shown in Fig. 5a, and vice versa.

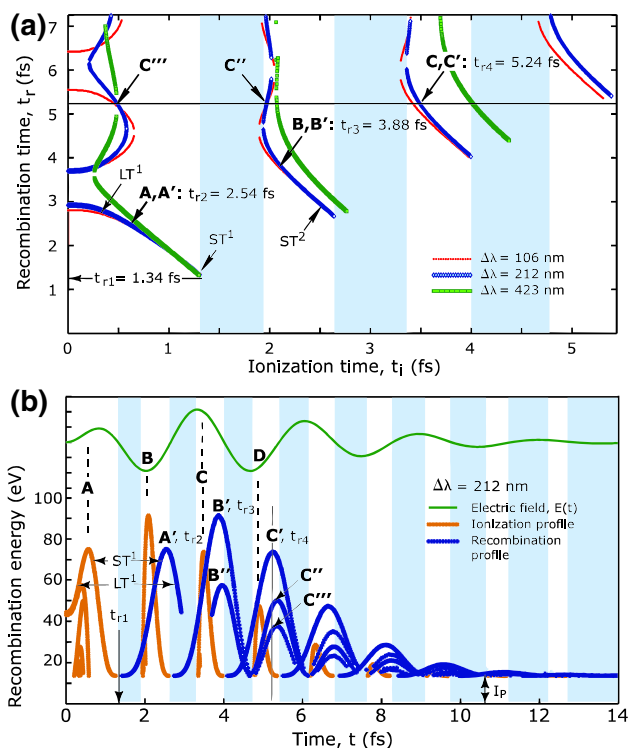


**Fig. 5** **a** Recombination time  $t_r$  in terms of the ionization time  $t_i$  of an electron, for  $\Delta\lambda = 106, 212,$  and  $423$  nm. **b** Kinetic energy of an electron at the recombination instant for the case of  $\Delta\lambda = 212$  nm. The plus sign and dark-blue curves represent directly the kinetic energy versus  $t_r$ . Besides, the x sign and orange curves show the recombination energy of the atom ionized at  $t_i$ . Solid curve is the electric field.  $I_p$  represents the ionization potential corresponding to 13.6 eV

### 2.2 Numerical method for high-order harmonic generation

As it was shown in the previous section, superposing several electric fields related to the CW beams resulted in

production of a linearly polarized electric field of a femtosecond pulse. Then, we can study the effects of these new designed pulses on the HHG in the hydrogen atom. After adjusting the electric field impacting on the target atoms, solution of the time dependent Schrödinger equation (TDSE) and finding the wave function of the electron, is the first step of this research. To study the dynamics of the electron under the influence of the electric field, TDSE is one of the most powerful methods. Especially here, we used a linearly polarized electric field along the  $z$  direction, thus, solving the TDSE in one dimension (1D-TDSE), along the  $z$  direction, is a good approximation to describing the HHG. So, we have

$$i \frac{\partial \psi(z, t)}{\partial t} = \hat{H} \psi(z, t) = \left[ -\frac{1}{2} \frac{\partial^2}{\partial z^2} + V(z) + zE(t) \right] \psi(z, t), \tag{7}$$

where  $\hat{H} = \hat{T}_z + U(z, t)$ ,  $\hat{T}_z = -(\partial^2 / \partial z^2) / 2$ , and  $U(z, t) = V(z) + zE(t)$ . Here,  $E(t)$  is linearly polarized electric field, and we used the soft-core potential  $V(z) = -(z^2 + \alpha)^{-1/2}$  to introduce the atomic potential.  $\alpha$  sets in the way to avoid singularities in the origin, and in this study is taken to be 1. In order to solve Eq. (7), in this paper we apply the split-operator method. For one step in the time scale, by a good approximation, we can rewrite Eq. (7) as  $\psi(z, t + \Delta t) \simeq \exp[-i \hat{H} \Delta t] \psi(z, t)$ , where the split operator method gives us

$$\begin{aligned} \psi(z, t + \Delta t) \simeq & \exp\left[-i \hat{T}_z \frac{\Delta t}{2}\right] \exp(-i U(z, t) \Delta t) \\ & \times \exp\left[-i \hat{T}_z \frac{\Delta t}{2}\right] \psi(z, t), \end{aligned} \tag{8}$$

and to avoid the spurious reflections at the walls of numerical window, the electron’s wave function is multiplied by a mask function of the form  $\cos^{1/8}$  in each time steps [47]. By the use of the approximation called Cayley form [30] and utilizing the finite difference method, the numerical solution of Eq. (8) is attainable. In the simulation, we set  $dz = 0.05$  a.u. in length and  $dt = 0.05$  a.u. in time scale. Thus, the wavefunction deduced from Eq. (8) is used for computing other physical quantities of interest. For example:

1. The influence of the initial norm in the wavefunction  $N_0(t)$  and instantaneous norm of the wave packet  $N(t)$  as

$$N_0(t) = \langle \psi_0(z, t) | \psi(z, t) \rangle, \tag{9}$$

$$N(t) = \langle \psi(z, t) | \psi(z, t) \rangle. \tag{10}$$

2. The ionization probability  $P(t)$ ,

$$P(t) = 1 - N(t). \tag{11}$$

Two equations above mean that any part of the wave function inside the calculation window is not considered ionized and still bound.

3. The laser-induced dipole moment and acceleration

$$d(t) = \langle \psi(z, t) | z | \psi(z, t) \rangle, \tag{12}$$

$$a(t) = -E - \langle \psi(z, t) | \frac{\partial V(z)}{\partial z} | \psi(z, t) \rangle. \tag{13}$$

4. The power spectrum of the high-order harmonics obtained from the absolute square of the Fourier transforms of the dipole acceleration  $a(t)$

$$S(\omega) = \left| \frac{1}{T} \int_0^T a(t) e^{-i\omega t} dt \right|^2, \tag{14}$$

where  $T = T_{\text{end}} + T_{\text{tail}}$  is the total duration of the pulse. Then, we can find the width-frequency distribution of high-order harmonics’ intensities, as it will be discussed in subsequent sections.

5. Time–frequency distributions of the harmonics’ intensities, defined by the Morlet-wavelet  $W[a] = w(\omega, t)$  of the dipole acceleration  $a(t)$  as [49, 50]

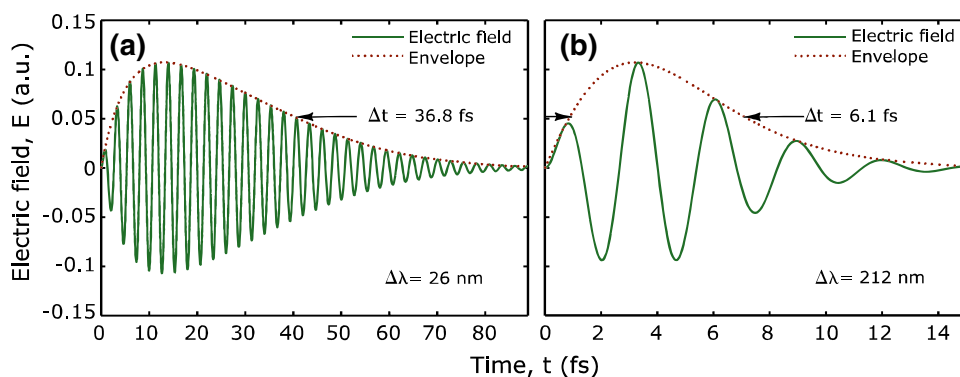
$$w(\omega, t) = \sqrt{\frac{\omega}{\sigma \sqrt{\pi}}} \int_0^t a(t') e^{-\frac{\omega^2(t-t')^2}{2\sigma^2}} e^{i\omega(t-t')} dt'. \tag{15}$$

Parameter  $\sigma$  is adjusted for the best balance between the resolutions in time and frequency domains and in this work it was chosen to be equal to  $2\pi$  for the best result. Some authors use the Gabor transform to show the time–frequency distribution of the harmonics’ intensities [51, 52], but in this study we preferred to use Morlet-wavelet transform, because it provides more details.

### 3 Numerical results

In the previous section, using a set of especially designed linearly polarized and naturally chirped electric fields, interacting with hydrogen gas as target, 1D-TDSE of this system is introduced. We planned to identify how these laser fields, affect the electron’s dynamics. In this section we will deliberate the impact results of these femtosecond pulses on the hydrogen atom. The set consists of 10 selected band-widths ( $\Delta\lambda$ ) from  $\Delta\lambda = 26$  to 476 nm. As mentioned previously, the spectral distribution has a Gaussian function centered

**Fig. 6** Electric fields of two typical femtosecond pulses produced from the Gaussian spectral distribution of width **a** 26 nm and **b** 212 nm



at  $\lambda_0 = 800$  nm and the color difference between the beams is set to be  $\delta\lambda = 0.5$  nm in this study. The scales of the time–distance window was adjusted to be 200 a.u. in the electronic coordinate and  $T_{\text{end}}$  for the time axis, related to the length of the electric field. During the 1D-TDSE simulation, to achieve a reasonably accurate results, we set  $dt = 0.05$  a.u. and  $dz = 0.05$  a.u. For example, in this section we study the effect of two types of these electric fields corresponding to  $\Delta\lambda = 212$  nm, and  $\Delta\lambda = 26$  nm to get a fair sense of distinctions. Figure 6 depicts these electric fields. In agreement with Fig. 3, we can see that broadening of the spectral width results in shortening the pulse width. Influence of these electric fields on the hydrogen atom affects the electron dynamics. Electronic probability density,  $\mathcal{P}(z, t) = |\psi(z, t)|^2$ , in Fig. 7, shows its dependency to the behavior of the electric field.

Using the wave function of the electron,  $\psi(z, t)$ , the parameters such as the instantaneous norm  $N(t)$ , the ionization probability,  $P(t) = 1 - N(t)$ , contribution of the initial wave function in evolution of the wave function,  $N_0(t)$ , dipole momentum,  $d(t)$ , and acceleration,  $a(t)$ , the power spectrum of high-order harmonics,  $S(t)$ , and also time–frequency distribution of high-order harmonics intensities, can be calculated. Figure 8 presents  $N_0(t)$ ,  $N(t)$ , and  $P(t)$  along with the classical ADK ionization rate [53] as a function of time for two cases of  $\Delta\lambda = 26$  and 212 nm. In Fig. 8a, c we have plotted the  $N_0(t)$  in the logarithmic time scale to see clearly how it drastically depletes at the beginning of the incident pulse. In Fig. 8b, d we can see the instantaneous norm of the wavefunction,  $N(t)$ , and ionization probability,  $P(t)$ . Presence of the ADK ionization rate curves along with  $N_0(t)$  and  $N(t)$  in Fig. 8 elucidates depletion manner of  $N_0(t)$  and  $N(t)$  with time. For example, in Fig. 8c it can be seen that each peak in ADK ionization rates such as  $A, B, \dots$ , (corresponds to a small mitigation in  $N_0(t)$ ). Existence of lots of peaks in the ADK ionization rate for the case when  $\Delta\lambda = 26$  nm associates to nearly complete alleviation of  $N_0$  and  $N$ , and vice versa for

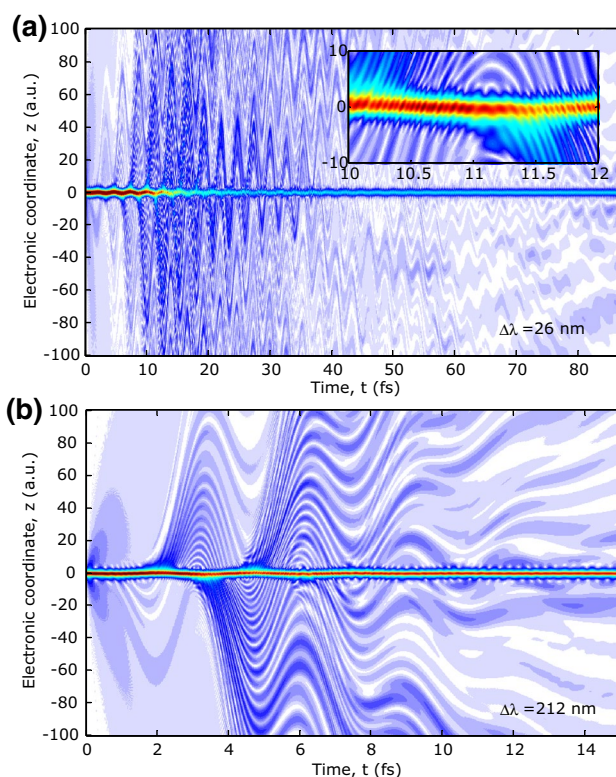


**Fig. 7** Probability density  $\mathcal{P}(z, t)$  of the presence of electron as a function of coordinate  $z$  and time  $t$  for **a**  $\Delta\lambda = 26$  nm and **b**  $\Delta\lambda = 212$  nm

$\Delta\lambda = 212$  nm. Also, a comparison with Fig. 6 shows that the most probable ionization process takes place when the laser electric field reaches its maximum. Figure 9 depicts the maximum ionization probability  $P_{\text{max}}$  versus  $1/\Delta\lambda$  calculated at the end of the pulse,  $T_{\text{end}}$  (without considering any extra tail), as is marked in Fig. 8, and the inset shows this probability versus  $\Delta\lambda$ . This figure shows that by increasing  $\Delta\lambda$ , maximum ionization probability decreased. It can easily be understood from the fact that the

**Fig. 8** **a, c** The norm of the initial wave function of the atomic hydrogen,  $N_0(t)$ ; **b, d** instantaneous norm,  $N(t)$ , and ionization probability,  $P(t)$ , of the atom, when  $\Delta\lambda = 26$  and 212 nm, respectively. ADK ionization rates are also included in these figures. The relation between the ADK ionization rate and  $N_0$  can be clearly seen in these figures

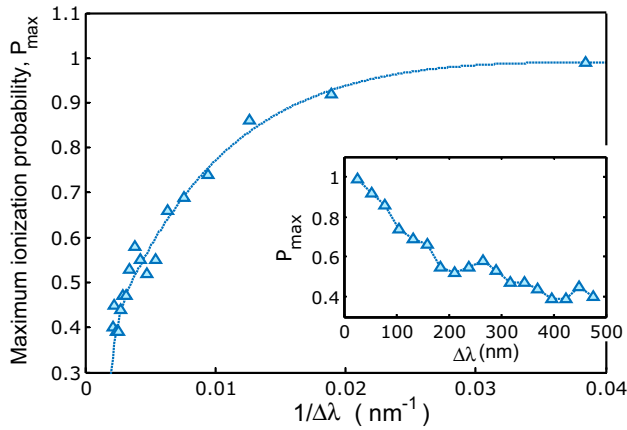
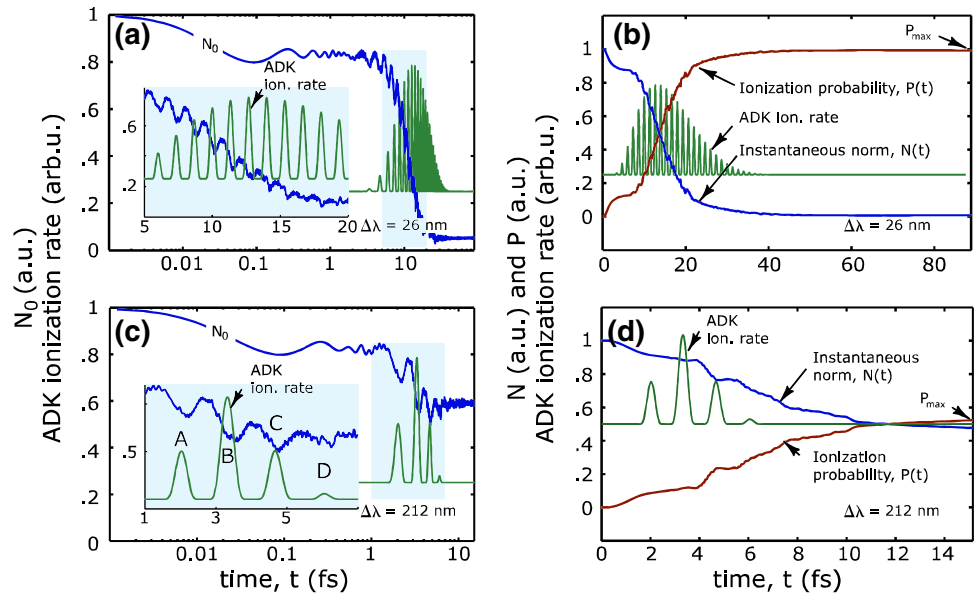


**Fig. 9** Maximum ionization probability ( $P_{\max}$ ) occurred at the  $T_{\text{end}}$  of the pulse, versus  $1/\Delta\lambda$ . Inset shows  $P_{\max}$  versus  $\Delta\lambda$

amplitudes of all the laser fields under the study have the same maximum, independent of the pulse duration. In other words, pulses with the smallest bandwidths are longer. Consequently, more laser cycles contribute to the total ionization. Therefore,  $P_{\max}$  must increase by decreasing  $\Delta\lambda$ . Figure 10 depicts the dipole momentum  $d(t)$  and acceleration  $a(t)$  for two cases of  $\Delta\lambda = 26$  nm and  $\Delta\lambda = 212$  nm. Using dipole acceleration and wave function of the electron,  $\psi(z,t)$ , and via Eq. (14) we can calculate the power spectrum of high-order harmonics. Behavioral illustration of power spectrum with respect to  $\Delta\lambda$  is depicted in Fig. 11. In Fig. 11a, for  $\Delta\lambda = 26$  nm, we have compared the harmonics spectrum related to two values of pulse intensities

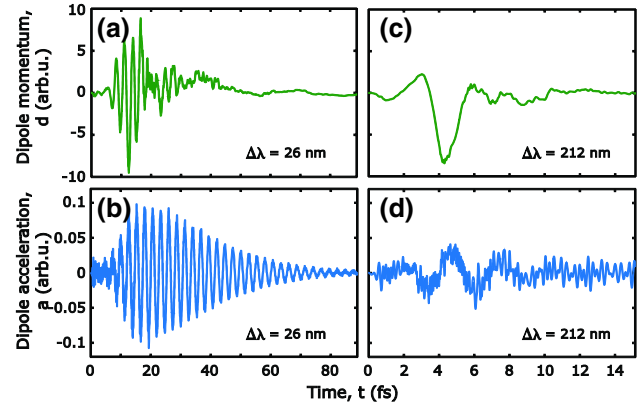


**Fig. 10** Dipole momentum, and acceleration of the electron in the external electric field of the femtosecond pulses corresponding to **a, b**  $\Delta\lambda = 26$  nm and **c, d**  $\Delta\lambda = 212$  nm, respectively. All the figures are plotted for the case when  $T_{\text{tail}} = 0$

corresponding to  $I_0 = 111$  TW/cm<sup>2</sup> (red-dashed curve), below the barrier ionization intensity, and  $I_0 = 400$  TW/cm<sup>2</sup> (blue-solid curve), over the barrier ionization intensity. It is seen that in this case of over barrier ionization, not only the cutoff energy does not become lower than the classical cutoff ( $I_p + 3.17 U_p$ ), but also, values of the harmonics power related to both values of intensities are almost the same. On the other hand, the broader plateaus of the harmonic spectrums are more favorable in this study, therefore, we can continue with laser pulses with the intensity of 400 TW/cm<sup>2</sup>. Since the pulse has a distributed wavelength spectrum, the ponderomotive energy  $U_p$  has a



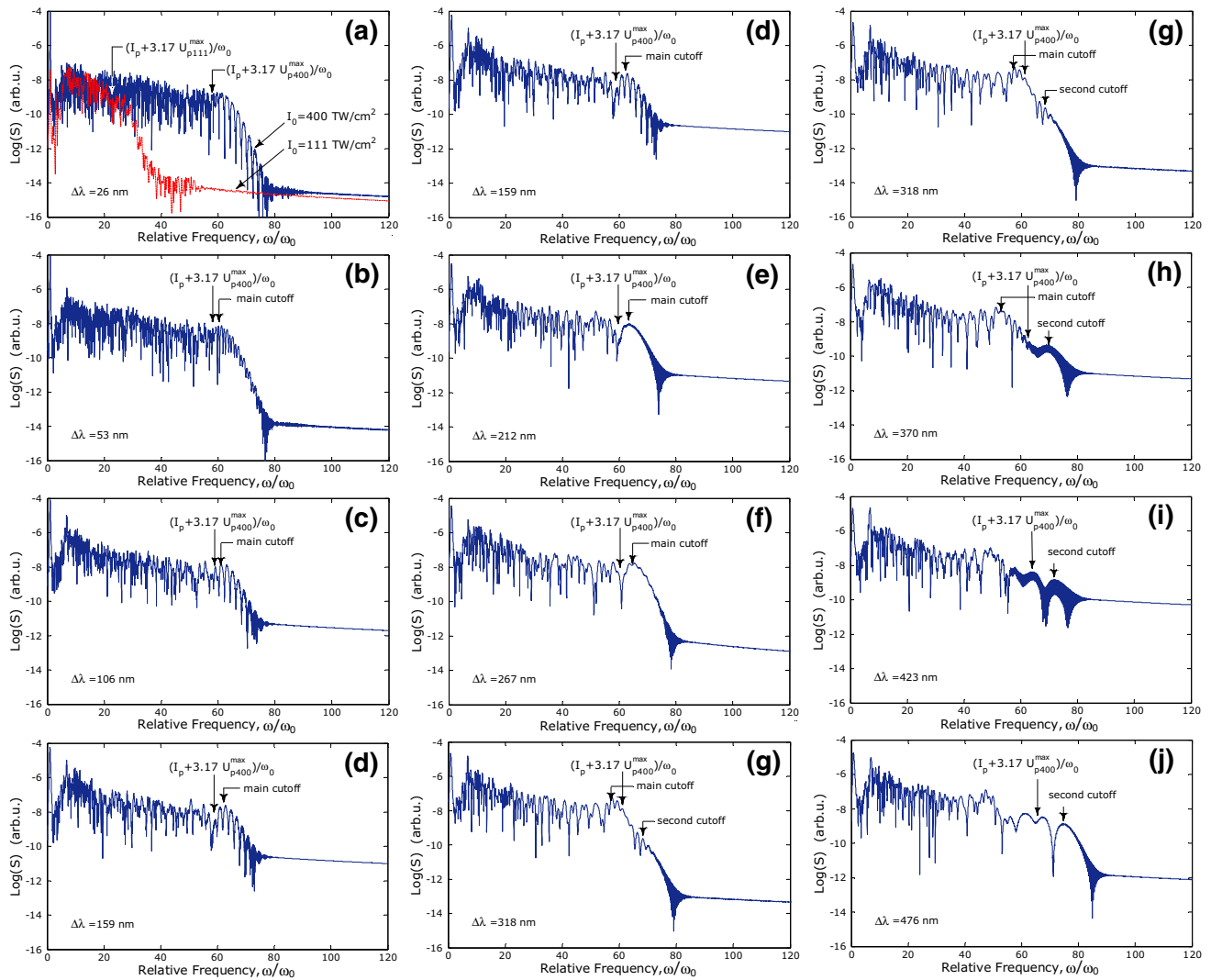
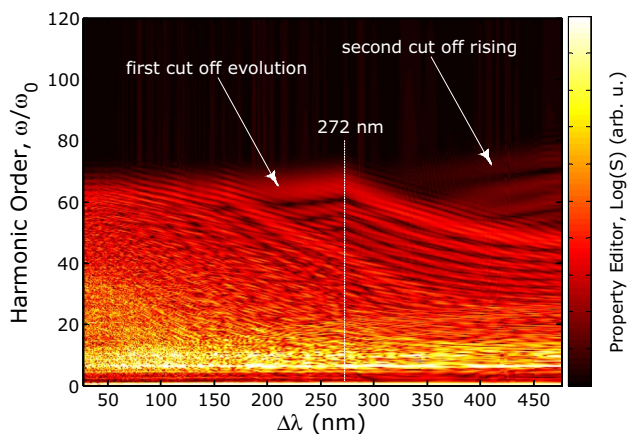


**Fig. 11** Power spectra of HHG using femtosecond pulses with 10 different  $\Delta\lambda$  from 26 to 476 nm, depicted in **a–j**, respectively. In **a** we compare the power spectrum that resulted from two different pulses with various intensities. *Red-dashed curve* corresponds to

$I_0 = 111 \text{ TW/cm}^2$  and *blue-solid curve* shows the power spectrum related to  $I_0 = 400 \text{ TW/cm}^2$ . In the rest of the figures  $I_0 = 400 \text{ TW/cm}^2$ . These figures show that the cutoff harmonic increases by increasing  $\Delta\lambda$ . In these figures  $\omega_0 = 0.057 \text{ a.u.}$  and  $T_{\text{tail}} = 0$

frequency distribution of  $U_p(\omega) = I(\omega)/4\omega^2$ , and because the distribution of its intensity has a peak,  $U_p$  also has a peak in the frequency distribution, and hence we cannot designate a certain frequency for introducing the classical cutoff for recombination energy ( $I_p + 3.17 U_p$ ). Thus, in this figure maximum classical cutoff is identified. Besides, it can be seen from Fig. 11 that the cutoff harmonics happens in a sense far from the classical prediction. Also, in Fig. 12 the width–frequency distribution of harmonics’ intensities can briefly be seen. Indeed, the vertical axis represents the harmonic spectrum, and the horizontal axis shows the width of the pulse,  $\Delta\lambda$ . In this figure, we can find that the cutoff frequency of the spectrum increases by  $\Delta\lambda$ .

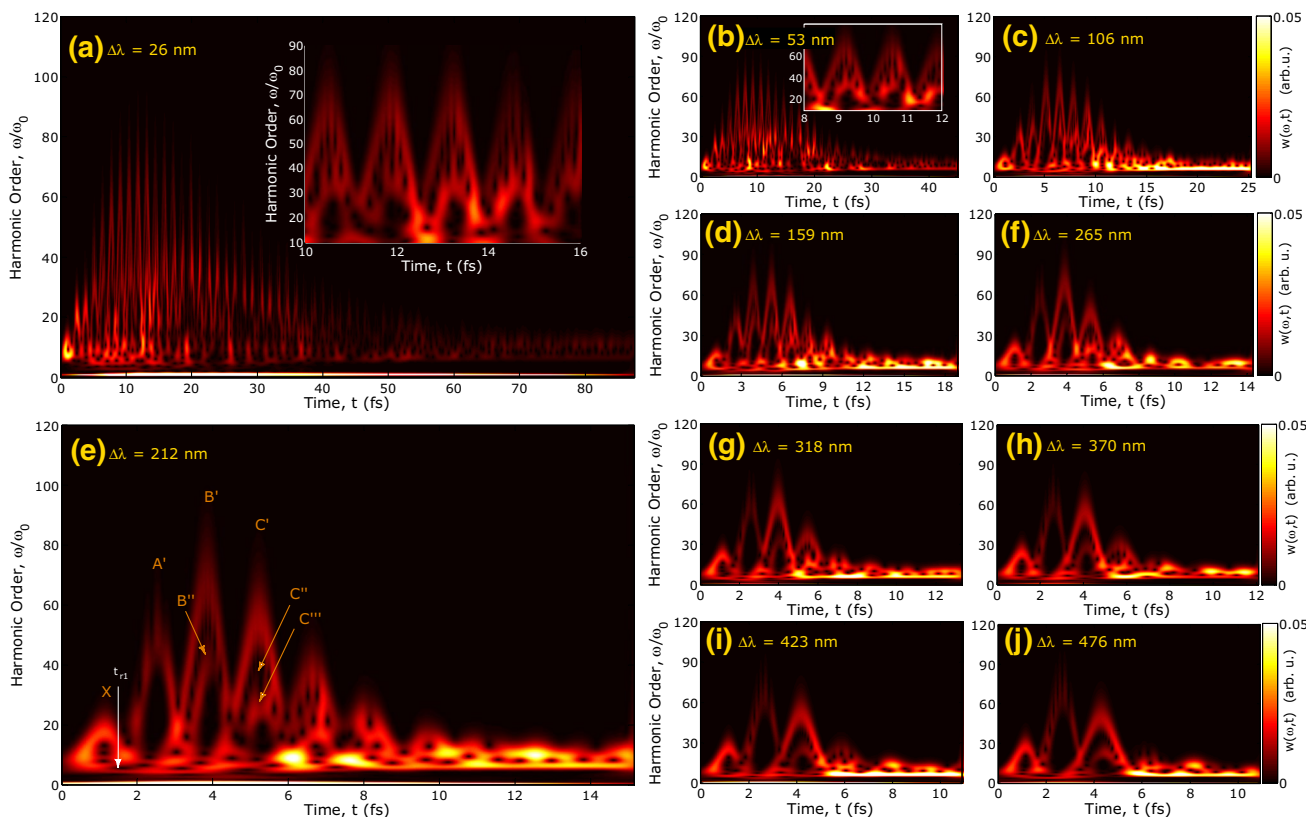
Furthermore, time–frequency distribution of the harmonics’ intensities can also be studied using the Morlet-wavelet transform introduced by Eq. (15). Figure 13 shows the time–frequency distribution of the harmonics intensities. Figure 13a–j is related to 10 especially produced broadband pulses of  $\Delta\lambda = 26\text{--}476 \text{ nm}$ , respectively. The horizontal axis shows the recombination time,  $t_r$ , and the vertical axis shows high-order harmonics of the central frequency  $\omega_0$ . In this figure, we can clearly see the trajectories of the electron. For example, Fig. 13e is related to Fig. 5b and we can compare these two figures. Although, Fig. 5 was deduced from classical theory, we can see a lot of similarities between these two figures. As mentioned



**Fig. 12** Width–frequency distribution of high-order harmonics powers. The main cutoff begins to reduce in  $\Delta\lambda = 272$  nm; instead the second cutoff grows up

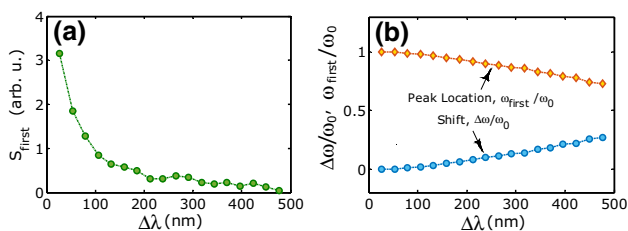
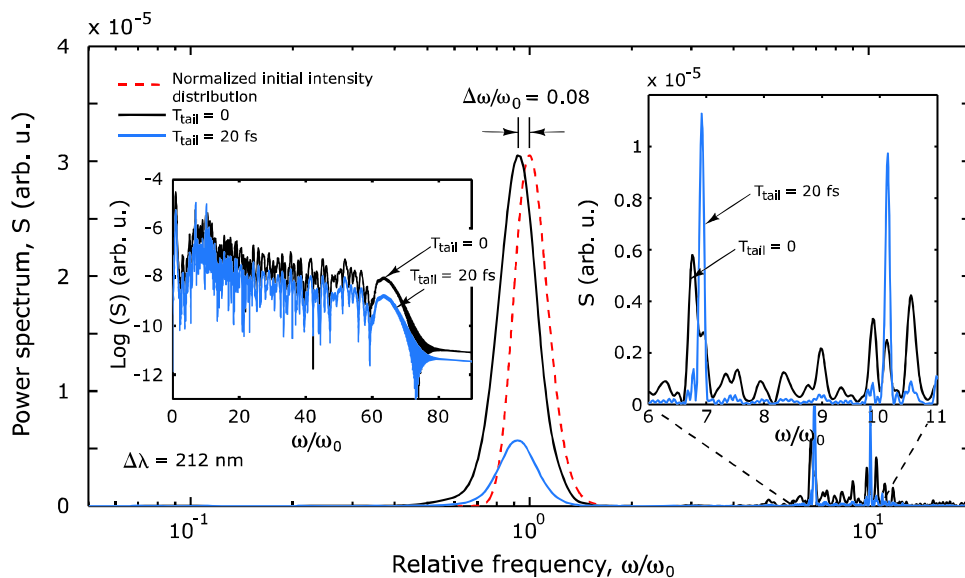
above, trajectories seen in Fig. 13e are related to the recombination profile in Fig. 5b, and it is expected that behaviors of the trajectories in these two figures be the same. For example, points A', B', C', etc., in Fig. 13e are related to the maximum recombination energies represented in

Fig. 5b. In addition, higher order trajectories of the electron such as B'', C'', C''', etc., can also easily be observed in Fig. 13e. However, there are some differences between these two figures, such as predicted in the recombination process before  $t_{r1}$ , represented by X in Fig. 13e. Classical theory could not predict this trajectory, whereas this trajectory is seen from solving the TDSE in quantum mechanical analysis. There are some interesting behaviors in the power spectrum deduced by these especial electric fields. To introduce these behaviors we review, for example, the HHG using the pulse with a spectral width of  $\Delta\lambda = 212$  nm from a different point of view. Figure 14 shows this spectrum again, but with the power axis in the linear scale. In the figure, it is indicated that the main frequency distribution (as the first harmonic), is re-generated by a little red-shift, about  $\Delta\omega/\omega_0 = 0.08$  from frequency distribution of the initial incident pulse. This red-shift might be because of some losses occurring during three steps of the process, such as possible radiations occurring during electron acceleration in the laser field, etc.; or because of the approximations that have been applied in the simulation technique, such as single-active-electron approximation and neglecting the motion of the nuclei during three steps of ionization



**Fig. 13** Time–frequency spectrum corresponding to 10 different femtosecond pulses by  $\Delta\lambda = 26$ –476 nm from a to j, respectively

**Fig. 14** Power spectrum of the pulse correspond to  $\Delta\lambda = 212$  nm for two cases of  $T_{\text{tail}} = 0$  (black solid line) and  $T_{\text{tail}} = 20$  fs (blue or gray solid line). Red dashed line represents the spectrum corresponding to the incident pulse. Left inset shows the whole generated spectrum in the logarithmic scale. Right inset shows clearly that intensities of two orders of harmonics are evidently larger, and their intensities grow up by the tail



**Fig. 15** **a** Peak intensity of the first harmonic; **b** first harmonic location, and its shift from the incidental pulse; versus  $\Delta\lambda$

till the recollision processes; or assuming that the electron is ionized by zero velocity, and so on. Another worthy of attention effect is growing two of the harmonics up by increasing the tail of the pulse. These harmonics are those generated at the initiation of the plateau. As is observed from Fig. 14, harmonics intensities related to  $\omega/\omega_0 = 6.92$  and  $10.14$  grown up by the tail of the pulse. It is more interesting to find that this effect can be seen for other values of  $\Delta\lambda$ . Figure 15a shows the peak intensity of the first generated harmonic spectrum, introduced by  $S_{\text{first}}$ , with respect to the spectral width of the pulse,  $\Delta\lambda$ . We have already mentioned that the first harmonics have a spectrum and are not in the exact frequency, because the incident femtosecond pulse has a spectrum. As is shown in Fig. 14, the first harmonics spectrum shifted from incident pulse. This shift increases versus  $\Delta\lambda$ , and is demonstrated in Fig. 15b. Figure 16 compares the cutoff order of the harmonics in the case of  $I_0 = 400$  TW/cm<sup>2</sup> with those related to  $I_0 = 111$  TW/cm<sup>2</sup>, versus  $\Delta\lambda$ . Figure 16a is related to  $I_0 = 111$  TW/cm<sup>2</sup>, below the barrier ionization region, and it can be seen that the classical prediction of the cutoff harmonic is somehow in agreement with the main cutoff

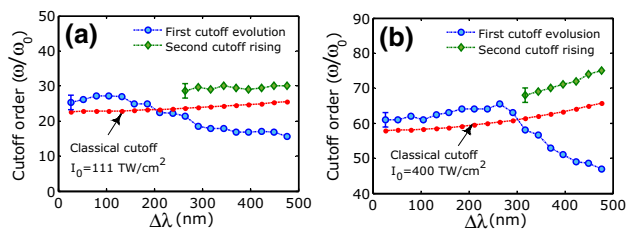


**Fig. 16** Cutoff order with respect to  $\omega_0$  for **a**  $I_0 = 111$  TW/cm<sup>2</sup>, and **b**  $I_0 = 400$  TW/cm<sup>2</sup>. Dashed horizontal line represents the classical cutoff prediction in both figures. In **a** the field intensity is below the barrier, and as can be seen, by increasing the pulse-width ( $\Delta\lambda$ ) the main cutoff reaches the classical calculation. **b** refers to the fact that in the over barrier ionization region, by increasing  $\Delta\lambda$ , cutoff order goes down far from the classic cutoff

deduced from TDSE solution, as mentioned in [48]. Figure 16b, deduced from Fig. 11 for the field intensity of  $I_0 = 400$  TW/cm<sup>2</sup>, in the over barrier ionization region. This figure can be compared with Fig. 12. As Fig. 12 shows, for  $\Delta\lambda = 272$  nm, the first cutoff begins to somehow reduction drastically; moreover, coincidentally, a growth to some larger harmonics is began. For the values of  $\Delta\lambda$  over 300 nm, the cutoff harmonic becomes lower than the classical analysis anticipation, similar that mentioned in [48] for over barrier ionization region. Although, the second rising cutoff continues the increasing behavior of the first cutoff, however, harmonics efficiency after the main cutoff drastically drops and the HHG process becomes inefficient [48, 54, 55]. Finally in Fig. 17 we show that the relative intensities of the first robust harmonics generated, i.e.,  $S_{6.92}/S_{\text{first}}$  and  $S_{10.14}/S_{\text{first}}$ , increase by the tail of the pulse. This figure is produced for three values of  $\Delta\lambda = 106, 212, 370$  nm.

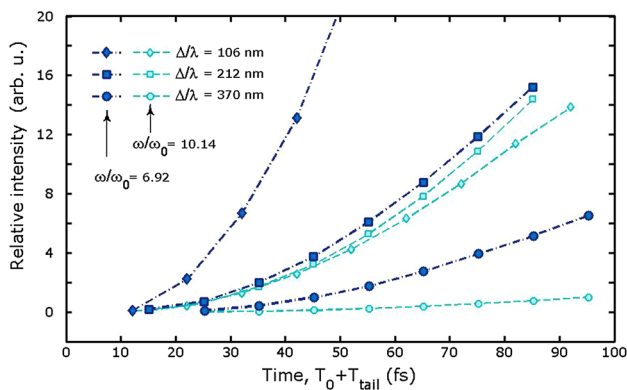


**Fig. 17** The relative intensity variation for two frequencies of 6.92  $\omega_0$  and 10.14  $\omega_0$  with respect to total duration of the pulse, i.e.,  $T_0 + T_{\text{tail}}$

## 4 Conclusions

In this article, we designed especial types of femtosecond laser pulses, through superposition of several CW beams with FWHM lower than 1 nm. There is a constant value, in the order of sub nm, of difference between the beams' color. The most important assumption is that these beams are locked at zero phase. This essential assumption is the only and enough condition to produce a femtosecond pulse through superposition of the beams. Also by considering a Gaussian distribution centered at 800 nm for amplitudes of the beams, we can have different pulses with various spectral widths and therefore with several pulse durations. In the study of high-order harmonic power spectrum, we needed to have some border plateaus. Thus, we decided to calculate the harmonics behaviors under the influence of some pulses by the intensities in the over barrier ionization region, i.e., we have set  $I_0 = 400 \text{ TW/cm}^2$ , where for hydrogen atom, barrier ionization intensity is  $I_b^H = 140 \text{ TW/cm}^2$ . Against to some investigations in the literature, some of these intense fields by  $\Delta\lambda$  below 300 nm, lead to the cutoff in agreement with the classical cutoff energy prediction ( $I_p + 3.17 U_p$ ). Also we found the minimum intensity of the field ( $I_0 = 111 \text{ TW/cm}^2$ ) to satisfy the Keldysh condition for tunneling ionization. Thus, willingly we used the higher intensity for this study. Two advantages of these pulses are: firstly, these pulses are produced without considering any pulse shaping processes, and secondly, these pulses have an intrinsic chirp effect that causes the harmonic spectrum to expand. After designing the pulses, we studied the behavior of hydrogen atom and specially dynamics of its electron under the influence of these types of femtosecond pulses. For example, wave function of the electron in external laser field, and consequently, ionization probability and norm of the wave-function have been investigated. Also, dipole momentum

and acceleration as well as the harmonics' spectrum and time–frequency distribution of the harmonics intensities are numerically analyzed. During these studies we observed two interesting subjects: (a) first extracted frequencies, which have a spectrum dependence on the incident pulse, have a red-shift from the incident pulse, and (b) for two frequencies at the beginning of the plateau, i.e.,  $\omega/\omega_0 = 6.92$  and 10.14, it is seen that their relative intensities, i.e.,  $S_{6.92}/S_{\text{first}}$  and  $S_{10.14}/S_{\text{first}}$ , grow up by the tail of the pulse. By increasing  $\Delta\lambda$ , it was shown that the cutoff frequency of the spectrum and the shift of the first harmonic from the incident pulse is increased. In addition, a decrease in the maximum ionization probability and in the first harmonic intensity was seen as a result of growing  $\Delta\lambda$ . Indeed in this article we studied the effect of a broadband femtosecond pulse on behavior of electron dynamics, and especially on high-order harmonics generation.

## References

1. P.B. Corkum, F. Krausz, *Nature Phys.* **3**, 381 (2007)
2. F. Krausz, M. Ivanov, *Rev. Mod. Phys.* **81**, 163 (2009)
3. P.M. Paul, E.S. Toma, P. Breger, G. Mullot, F. Auge, Ph Balcou, H.G. Muller, P. Agostini, *Science* **292**, 1689 (2001)
4. M. Hentschel, R. Kienberger, Ch. Spielmann, G.A. Reider, N. Milosevic, T. Brabec, P. Corkum, U. Heinzmann, M. Drescher, F. Krausz, *Nature* **414**, 509 (2001)
5. J.L. Krausz, K.J. Schafer, K.C. Kulander, *Phys. Rev. Lett.* **68**, 3535–3538 (1992)
6. P.B. Corkum, *Phys. Rev. Lett.* **71**, 1994 (1993)
7. T. Zuo, S. Chelkowski, A.D. Bandrauk, *Phys. Rev. A* **48**, 3837 (1993)
8. M. Lewenstein, Ph Balcou, MYu. Ivanov, Anne L'Huillier and P. B. Corkum. *Phys. Rev. A* **49**, 2117 (1994)
9. A. McPherson, G. Gibson, H. Jara, U. Johann, T.S. Luk, I.A. McInntyre, K. Boyer, C.K. Rhodes, *J. Opt. Soc. Am. B* **4**, 595 (1987)
10. X.F. Li, A. L'Huillier, M. Ferray, L.A. Lompré, G. Mainfray, *Phys. Rev. A* **39**, 5751 (1989)
11. J. Itatani, J. Levesque, D. Zeidler, H. Niikura, H. Pépin, J.C. Kieffer, P.B. Corkum, D.M. Villeneuve, *Nature* **432**, 867 (2004)
12. R. de Nalda, E. Heesel, M. Lein, N. Hay, R. Velotta, E. Springate, M. Castillejo, J.P. Marangos, *Phys. Rev. A* **69**, 031804 (2004)
13. Xiaofan Zhang, Yang Li, Xiaosong Zhu, Qingbin Zhang, Pengfei Lan, Lu Peixiang, *J. Phys. B* **49**, 015602 (2016)
14. R. Ganeev, M. Suzuki, M. Baba, H. Kuroda, T. Ozaki, *Opt. Lett.* **30**, 768 (2005)
15. R.A. Ganeev, L.B. Elouga Bom, J. Abdul-Hadi, M.C.H. Wong, J.P. Brichta, V.R. Bhardwaj, T. Ozaki, *Phys. Rev. Lett.* **102**, 013903 (2009)
16. R.A. Ganeev, C. Hutchison, T. Witting, F. Frank, W.A. Okell, A. Zair, S. Weber, P.V. Redkin, D.Y. Lei, *J. Phys. B At. Mol. Opt. Phys.* **45**, 165402 (2012)
17. D. von der Linde, T. Engers, G. Jenke, P. Agostini, G. Grillon, E. Nibbering, A. Mysyrowicz, A. Antonetti, *Phys. Rev. A* **52**, R25 (1995)
18. B. Dromey, M. Zepf, A. Gopal, K. Lancaster, M.S. Wei, K. Krushelnick, M. Tatarakis, N. Vakakis, S. Moustazis, R. Kodama, M.

- Tampo, C. Stoeckl, R. Clarke, H. Habara, D. Neely, S. Karsch, P. Norreys, *Nat. Phys.* **2**, 456 (2006)
19. T.T. Luu, H.J. Worner, *Phys. Rev. B* **94**, 115164 (2016)
  20. S.I. Simonsen, S.A. Sørngard, M. Førre, J.P. Hansen, *J. Phys. B At. Mol. Opt. Phys.* **47**, 065401 (2014)
  21. S. Ghimire, A.D. DiChiara, E. Sistrunk, P. Agostini, L.F. DiMauro, D.A. Reis, *Nat. Phys.* **7**, 138–141 (2011)
  22. S. Ghimire, A.D. DiChiara, E. Sistrunk, G. Ndabashimiye, U.B. Szafruga, A. Mohammad, P. Agostini, L.F. DiMauro, D.A. Reis, *Phys. Rev. A* **85**, 043836 (2012)
  23. A.D. Bandrauk, S. Chelkowski, D.J. Diestler, J. Manz, K.-J. Yuan, *Phys. Rev. A* **79**, 023403 (2009)
  24. R.M. Potvliege, N.J. Kylstra, C.J. Joachain, *J. Phys. B* **33**, L743 (2000)
  25. F. Hosseinzadeh, S. Batebi, M.Q. Soofi, *J. Exp. Theo. Phys.* **124**, 379–387 (2017)
  26. M. Vafae, H. Sabzyan, Z. Vafae, A. Katanforoush, *Phys. Rev. A* **74**, 043416 (2006)
  27. H. Ahmadi, A. Maghari, H. Sabzyan, A.R. Niknam, M. Vafae, *Phys. Rev. A* **90**, 043411 (2014)
  28. A.D. Bandrauk, S. Chelkowski, S. Kawai, H. Lu, *Phys. Rev. Lett.* **101**, 153901 (2008)
  29. I. Yavuz, Y. Tikman, Z. Altun, *Phys. Rev. A* **92**, 023413 (2015)
  30. V.T. Platonenko, A.F. Sterjantov, V.V. Strelkov, *Laser Phys.* **13**, 443 (2003)
  31. Hassan Sabzyan, Mohsen Vafae, *Phys. Rev. A* **71**, 063404 (2005)
  32. K. Liu, W. Hong, Q. Zhang, P. Lu, *Opt. Exp.* **19**, 26359 (2011)
  33. Y. Zheng, Z. Zeng, R. Li, Z. Xu, *Phys. Rev. A* **85**, 023410 (2012)
  34. D.B. Milošević, *J. Phys. B* **48**, 171001 (2015)
  35. D.B. Milošević, *Phys. Rev. A* **92**, 043827 (2015)
  36. H. Sabzyan, S.H. Ahmadi, M. Vafae, *J. Phys. B* **47**, 105601 (2014)
  37. M. Lein, N. Hay, R. Velotta, J.P. Marangos, P.L. Knight, *Phys. Rev. A* **18**, 183903 (2002)
  38. M. Lein, N. Hay, R. Velotta, J.P. Marangos, P.L. Knight, *Phys. Rev. Lett.* **88**, 183903 (2002)
  39. L. Feng, *Phys. Rev. A* **92**, 053832 (2015)
  40. J.J. Carrera, Shih-I Chu, *Phys. Rev. A* **75**, 033807 (2007)
  41. L. Feng, T. Chu, *Phys. Rev. A* **84**, 053853 (2011)
  42. R.-F. Lu, H.-X. He, Y.-H. Guo, K.-L. Han, *J. Phys. B* **42**, 225601 (2009)
  43. Haixiang He, Lu Ruifeng, Peiyu Zhang, Yahui Guo, Keli Han, Guozhong He, *Phys. Rev. A* **84**, 033418 (2011)
  44. F. He, C. Ruiz, A. Becker, *Phys. Rev. Lett.* **99**, 083002 (2007)
  45. I. Yavuz, M.F. Ciappina, A. Chacon, Z. Altun, M.F. Kling, M. Lewenstein, *Phys. Rev. A* **93**, 033404 (2016)
  46. N.-T. Nguyen, V.-H. Hoang, V.-H. Le, *Phys. Rev. A* **88**, 023824 (2013)
  47. A.D. Bandrauk, J. Manz, K.-J. Yuan, *Laser Phys.* **19**, 1559–1573 (2009)
  48. P. Moreno, L. Plaja, V. Malyshev, and L. Roso, *Phys. Rev. A* **51**, 4746–4753 (1995)
  49. C. Chandre, S. Wiggins, T. Uzer, *Phys. D* **181**, 171 (2003)
  50. A.D. Bandrauk, S. Chelkowski, H. Lu, *Chem. Phys.* **414**, 73 (2013)
  51. A.D. Bandrauk, S. Chelkowski, H. Lu, *J. Phys. B At. Mol. Opt. Phys.* **42**, 075602 (2009)
  52. C.C. Chirila, I. Dreissigacker, E.V. van der Zwan, M. Lein, *Phys. Rev. A* **81**, 033412 (2010)
  53. M.V. Ammosov, N.B. Delone, V.P. Krainov, *Sov. Phys. JETP* **64**, 1191–1194 (1986)
  54. V.V. Strelkov, A.F. Sterjanov, N. Yu Shubin, V.T. Platonenko, *J. Phys. B At. Mol. Opt. Phys.* **39**, 577–589 (2006)
  55. J.A. Pérez-Hernández, M.F. Ciappina, M. Lewenstein, A. Zaïr, L. Roso, *Eur. Phys. J. D.* **68**, 195 (2014)